ORIGINAL RESEARCH ARTICLE

Performance evaluation of non-water absorption coefficient partitioning algorithms in optically complex coastal waters of Kochi and Goa, India

Srinivas Kolluru*, Shirishkumar S. Gedam, Arun B. Inamdar

Centre of Studies in Resources Engineering, Indian Institute of Technology, Bombay, India

Abstract   Absorption coefficient partitioning algorithms (APAs) were developed to partition the total absorption coefficient ($a(\lambda)$) or total non-water absorption coefficient ($a_{nw}(\lambda)$) into the absorption subcomponents, i.e., absorption due to phytoplankton $a_{ph}(\lambda)$, colored dissolved organic matter (CDOM) $a_g(\lambda)$ and non-algal particulate matter $a_d(\lambda)$, λ is the wavelength. Absorption coefficients of CDOM and non-algal particulate matter are generally combined due to a similarity in exhibited spectral shape and represented as colored detrital matter (CDM) absorption coefficient, $a_{dg}(\lambda)$. This study focuses on the applicability of five APAs Schofield's, Lin's, Zhang's, Stacked Constraints Model (SCM) and Generalized Stacked Constraints Model (GSCM), in deriving the absorption subcomponents from $a_{nw}(\lambda)$ in optically complex coastal waters of Kochi and Goa, India. The average spectral Mean Absolute Percentage Errors (MAPE) obtained for all models in the retrieval of $a_{ph}(\lambda)$, $a_d(\lambda)$, $a_g(\lambda)$ and $a_{dg}(\lambda)$ lie in the ranges of 26—44%, 37—45%, 34—65% and 42—56%. Slopes of $a_{dg}(\lambda)$, $a_g(\lambda)$ and $a_d(\lambda)$ as indicated by S_{dg}, S_g and S_d are derivable from GSCM, Schofield and Lin's models only. GSCM model exhibited good retrieval capability of S_d with MAPE values of 22% and a correlation coefficient of 0.74. In retrieval of S_g parameter, none of the models demonstrated satisfactory performance. Overall, the GSCM and Schofield's models demonstrated good performance in the retrieval of absorption subcomponents, $a_{ph}(\lambda)$, $a_{dg}(\lambda)$, $a_d(\lambda)$ and S_d. Effect of applying baseline correction to $a_d(\lambda)$ on model

* Corresponding author at: Centre of Studies in Resources Engineering, Indian Institute of Technology Bombay, 400076 India.
E-mail address: savinirs.milas@gmail.com (S. Kolluru).

performance is studied. Tuning with *in situ* data can further improve the absorption subcomponent and slope parameter retrieval capability of the models.

1. Introduction

The optical properties of dissolved and particulate materials are known as Inherent Optical Properties (IOPs). IOPs are independent of the light field and are dependent on the substances present in the aquatic medium. Along with the incoming light field at the water surface, IOPs determine the light field's availability in the ocean. Total spectral light absorption coefficient $a(\lambda)$ [m^{-1}] is one of the widely studied IOPs of an aquatic medium (λ denotes wavelength) (Zaneveld, 2013). In all-natural waters except in waters of extreme turbid nature[1], $a(\lambda)$ can be expressed as the sum of absorptions from the optically significant substances (OSC), i.e., phytoplankton $a_{ph}(\lambda)$ [m^{-1}], non-algal particulate matter (NAP) $a_d(\lambda)$ [m^{-1}] and colored dissolved organic matter (CDOM) $a_g(\lambda)$ [m^{-1}] and water $a_w(\lambda)$ [m^{-1}] itself (Twardowski et al., 2018). The OSCs modify the light field available in the upper parts of the ocean and play an essential role in the biological and biogeochemical processes. Phytoplankton absorbs light for photosynthesis (primary production) wherein the light is converted to chemical energy and inorganic carbon to organic carbon. They form the base of the aquatic food chain and regulate CO_2 exchanges between the atmosphere and ocean along with other physical processes (Brewin et al., 2015; Zheng and Stramski, 2013a). Phytoplankton absorption is used to calculate phytoplankton productivity and provides information on chlorophyll-*a* concentration (Bricaud et al., 1998). Further, information about the phytoplankton community structure, taxonomy and size classes based on the absorption properties of pigments present in different groups can be derived from phytoplankton absorption (Ciotti and Bricaud, 2006; Ciotti et al., 2002; Uitz et al., 2008). The concentration of CDOM, the colored part of the dissolved organic matter (DOM), represents a dynamic part of the dissolved organic carbon pool and drives aquatic photochemistry with implications to biogeochemical processes such as carbon cycling. CDOM influences the upper water column photo processes and affects light and nutrient availability (Twardowski et al., 2004). CDOM, along with the non-algal particulate matter present in the water, absorbs the blue wavelengths of the visible spectrum and affects the photosynthesis of phytoplankton. CDOM exhibits a distinct spectral variability based on its source (terrestrial and marine-

derived) and different degradation pathways like microbial or photodegradation (Grunert et al., 2018). In coastal waters, the CDOM absorption and CDOM slope coefficient (S_g) exhibit distinct spectral features that provide information on the degradation state and presence of terrestrial biomarkers. NAP refers to particulate material that does not have extractable pigments. It includes all living and organic matter such as non-pigmented portion of phytoplankton cells, detritus, heterogenic bacteria, viruses and minerogenic particles. It also includes inorganic material of both biogenic (e.g., calcite liths and shells) and terrestrial origin (e.g., sand, silts and clay) (Mobley, 2010). NAP plays a key role in remineralisation and particulate matter movement (Zheng and Stramski, 2013a). The measurements of the a_d and a_g are essential in coastal regions especially, where both CDOM and NAP do not covary necessarily with chlorophyll-*a* concentration owing to coastal upwelling and riverine input of terrestrial organic and non-organic matter.

With technological advancements in optical sensors and devices, the absorption measurements of $a(\lambda)$ or total non-water absorption coefficient, $a_{nw}(\lambda)$ (total absorption coefficient after removal of the pure water absorption coefficient, $a_w(\lambda)$) can be derived or measured from various platforms such as satellites, *in situ* moorings, autonomous underwater vehicles and flow-through devices. The pure water absorption coefficient is assumed to be known within 2% in the visible wavelength range (Mason et al., 2016; Pope and Fry, 1997). Along with traditional filter pad absorption methods, devices like ac-9 (ac Meter Protocol Document, 2011), ac-s (Freeman, 2012), absorption sphere (a-sphere) (Dana and Maffione, 2006), Point Source Integrating Cavity Absorption Meter (PSICAM) (Röttgers et al., 2007) and flow-through PSICAM (Wollschläger et al., 2013) are capable of providing multispectral and hyperspectral absorption measurements in visible wavelength region with a high spectral resolution of ~1 nm.

Absorption coefficient partitioning algorithms (APAs) were developed to partition $a(\lambda)$ or $a_{nw}(\lambda)$ derived either from satellite imagery or absorption measurement devices. One category of APAs partition $a_{nw}(\lambda)$ or $a(\lambda)$ into $a_{ph}(\lambda)$, $a_d(\lambda)$, $a_g(\lambda)$ (Lin et al., 2013; Schofield et al., 2004; Zheng et al., 2015) or into $a_{ph}(\lambda)$ and $a_{dg}(\lambda)$, the combined absorption coefficient of CDOM and NAP material, hereafter referred to as colored detrital matter (CDM) (Ciotti and Bricaud, 2006; Oubelkheir et al., 2007; Roesler et al., 1989; Zhang et al., 2015). APAs have been used to study the spatiotemporal variations in phytoplankton size classes (Zhang et al., 2015), CDOM absorption coefficient at global scales (Bricaud et al., 2012) and in the retrieval of chlorophyll-*a* concentration in complex estuaries (Zheng and Digiacomo, 2017). Although the existing APAs were validated over waters covering a wide range of optical properties, their applicability to coastal, estuarine and

---

[1] The additive nature of IOPs is valid with an assumption that the OSC in water medium are discrete. The term "Discrete" refers to particles not being too close in proximity, typically must be separated by at least three times the radii of particles or interference in scattering properties. This condition is fulfilled in natural waters except in extremely turbid waters, where the suspended particles are very close to each other, thereby additive nature of IOPs does not hold true (Twardowski et al., 2018).

complex estuarine systems needs to be assessed for every region. Hence, the present study focuses on the applicability of these APAs in deriving the absorption subcomponents from $a_{nw}(\lambda)$ measured in coastal waters of Kochi and Goa, India. In addition to the magnitude of the absorption coefficients, the slope coefficients S_g, S_d and S_{dg} derived from the models that correspond to the shapes of the $a_g(\lambda)$, $a_d(\lambda)$ and $a_{dg}(\lambda)$ were compared. The five APAs evaluated are 1) Schofield's model (Schofield et al., 2004); 2) Lin's model (Lin et al., 2013); 3) Stacked Constraints Model (Zheng and Stramski, 2013a); 4) Generalized Stacked Constraints Model (Zheng et al., 2015) and 5) Zhang's model (Zhang et al., 2015). The five APA's follow different methodologies for retrieving the absorption subcomponents involving optimization, linear matrix inversion and constraint-based approaches. Further, the two sites (Kochi and Goa) differ in their optical characteristics due to the presence of the OSCs in various concentrations and compositions. Statistical indicators like mean absolute percentage error (MAPE), mean absolute error (MAE), root mean square deviation (RMSD) etc. were used for comparison of the APAs to assess their capability in the retrieval of absorption subcomponents from $a_{nw}(\lambda)$ measured in optically complex waters.

2. Data and methods

2.1. Data

The data used for comparing the performance of absorption decomposition algorithms were collected under the Satellite Coastal and Oceanographic Research (SATCORE) program by Indian National Centre for Ocean Information Services (INCOIS), Hyderabad, India (Lotliker et al., 2016). Under this program, the IOP data was collected at various coastal waters around India. For the present study, coincident measurements of the absorption subcomponents, $a_{ph}(\lambda)$, $a_d(\lambda)$ and $a_g(\lambda)$ were obtained in the wavelength range of 350−750 nm. The locations of sampling sites are shown in Figure 1.

Water samples were collected from the coastal waters of Kochi from January to December 2010−2013 (except July owing to a peak of southwest monsoon and associated high water current) (Souda et al., 2020). CDOM absorption coefficient, $a_g(\lambda)$ was measured spectrophotometrically following the procedure of Kowalczuk and Kaczmarek (1996). Briefly, water samples were filtered through a 0.2-μm cellulose nitrate membrane filter. Using Milli-Q type-I water as a blank, sample transparency was measured in 10-cm quartz cuvette in Shimadzu double-beam UV-2450 spectrophotometer in 200−750 nm wavelength range at 1-nm resolution.

Measured optical density (OD) is converted to $a_g(\lambda)$ using Eq. (1). Correction for scattering due to small particles and colloids that pass through filter paper is performed by subtracting $a_g(750)$ from the entire spectrum (Green and Blough, 1994). The spectral absorption coefficient was normalized with respect to 440 nm, given as Eq. (2)

$$a_g(\lambda) = 2.303 \ x \ OD(\lambda) x \ 100 \left[m^{-1} \right] \tag{1}$$

$$a_g(\lambda) = a_g(440) \ x \ exp \left[-S_g(\lambda - 440) \right] \left[m^{-1} \right] \tag{2}$$

where L is cuvette length in m, S_g is calculated by fitting a nonlinear exponential model between $a_g(\lambda)$ and wavelengths in the 400−750 nm range (Bricaud et al., 1981; Das et al., 2017; Twardowski et al., 2004) using a MATLAB code (Boss, 2014). For $a_p(\lambda)$ measurements, quantitative filter technique (QFT) was followed (Kishino et al., 1985; Mitchell, 1990). Water samples were filtered through Whatman GF/F membrane filters with 25 mm diameter and 0.7 μm pore size. The optical density is measured using Shimadzu double-beam UV-2450 spectrophotometer from 400−750 nm range with 1 nm resolution (90% acetone as blank). Absorption due to NAP ($a_d(\lambda)$) measurements were made after depigmentation of filtrate by using methanol. Following equations were used to calculate $a_{ph}(\lambda)$, $a_d(\lambda)$ and $a_{ph}(\lambda)$:

$$OD_s(\lambda) = 0.378 \ OD_f(\lambda) + 0.523 \left[OD_f(\lambda) \right]^2 \tag{3}$$

$$a_p(\lambda) = \frac{[2.303 \ x \ OD_s(\lambda)]}{\frac{V}{S_a}} \left[m^{-1} \right] \tag{4}$$

$$a_d(\lambda) = \frac{[2.303 \ x \ OD_s(\lambda)]}{\frac{V}{S_a}} \left[m^{-1} \right] \text{ (after depigmentation)} \tag{5}$$

$$a_{ph}(\lambda) = a_p(\lambda) - a_d(\lambda) \tag{6}$$

where $OD_s(\lambda)$ is the optical density of the particulate matter and NAP in suspension, $OD_f(\lambda)$ is the optical density of the particulate matter and NAP in a filter, V is filtration volume in m³, S_a is filtration area in m². The coefficients in Eq. (3) are path length correction factors (β factors) used to correct for multiple scattering in the glass fibre filters (Cleveland and Weidemann, 1993; Kyewalyanga et al., 1998). A detailed description of IOP measurements in Kochi coastal waters is presented in Minu et al. (2016, 2015, 2014) and Souda et al. (2020). In the case of Goa coastal waters, the same procedure is followed (as in Kochi) for obtaining the absorption coefficients but with Shimadzu UV-2550 spectrophotometer (Shimadzu Corporations, Japan) (Menon et al., 2005; Menon and Adhikari, 2018). The Goa site's IOP data were collected during March, May, September, October, November and December of 2013. The number of sample points from Kochi and Goa sites are 104 and 27, respectively.

Spectral absorption subcomponents, a_{ph}, a_d and a_g collected from Kochi and Goa coastal waters are presented in Figure 2 for the wavelength range of 400−750 nm. A total of 131 IOP measurements from Kochi and Goa coastal waters at seven light wavelengths corresponding to 412, 443, 469, 490, 510, 555, and 670 nm are subsets to compare the APA's. These wavelengths are present in most ocean color sensors starting from SeaWiFS to the latest Ocean and Land Color Imager of Sentinel-3 and the upcoming Ocean Color Monitor of the OceanSat-3 satellite.

The Kochi coastal waters are dominated by phytoplankton and NAP material with $a_{ph}(443)$ and $a_d(443)$ ranges of 0.032−1.121 m⁻¹ and 0.041−0.802 m⁻¹ respectively, as compared to CDOM absorption with $a_g(443)$ range of 0.003−0.043 m⁻¹. In the case of Goa coastal waters, the variations in phytoplankton, CDOM and NAP material absorption coefficients vary in the ranges of 0.023−0.198 m⁻¹, 0.058−1.506 m⁻¹ and 0.000−0.517 m⁻¹ respectively.
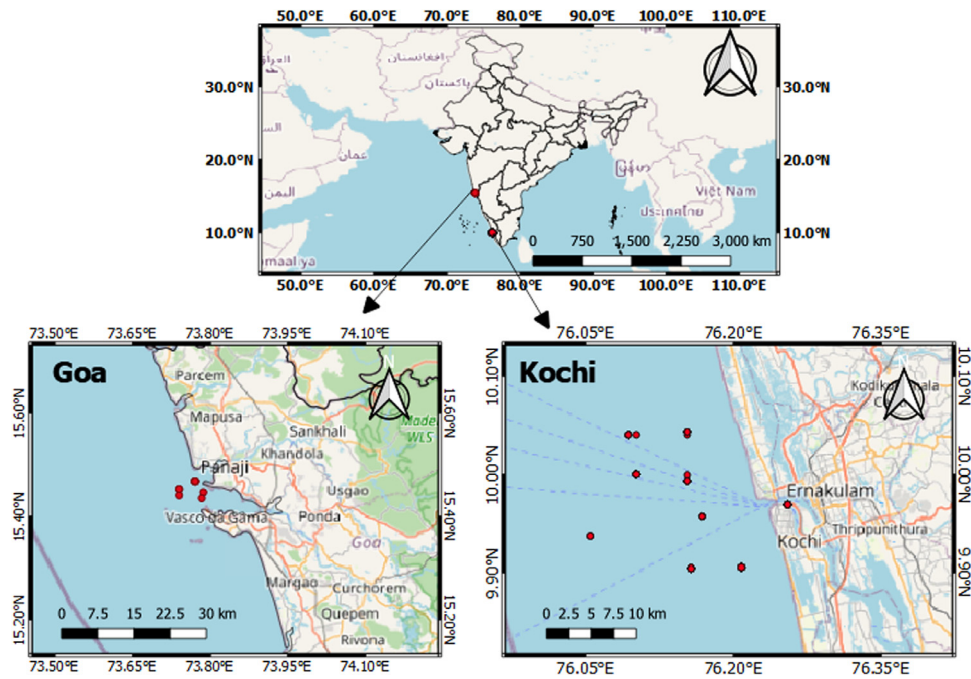
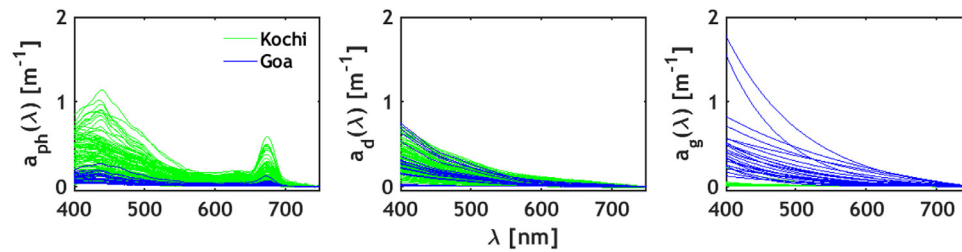**Figure 1**   Locations of sampling sites shown as red dots in coastal waters of Goa and Kochi, India.

Figure 2   Variability of $a_{ph}(\lambda)$, $a_d(\lambda)$ and $a_g(\lambda)$ for the 131 measurements from Kochi (green curves) and Goa (blue curves) in the wavelength range of 400—750 nm. Kochi waters are dominated by phytoplankton and NAP material, as indicated by higher magnitudes of $a_{ph}(\lambda)$ and $a_d(\lambda)$, as compared to $a_g(\lambda)$. Goa waters are dominated by NAP and CDOM, as compared to phytoplankton.

The mangrove-rich Mandovi-Zuari estuarine system in Goa coastal waters contributes to higher CDOM via freshwater discharge and tidal interaction (Menon et al., 2011; Nimit et al., 2016).

The ratio of CDM to phytoplankton absorption coefficient at 443 nm, $a_{dg}(443) : a_{ph}(443)$ ranges from 0.149—26.123. The NAP to phytoplankton ratio ($a_d : a_{ph}$) and CDOM to phytoplankton ($a_g : a_{ph}$) ratio at 443 nm range from 0.019—13.023 and 0.004 to 19.45, respectively. The blue-to-red band ratio for phytoplankton, $a_{ph}(443) : a_{ph}(670)$, ranges from 1.222 to 29.199. Similar to S_g, the values of S_d and S_{dg} are calculated by fitting a nonlinear exponential fit (Bricaud et al., 1981; Das et al., 2017; Twardowski et al., 2004) using a MATLAB code (Boss, 2014). The wavelength range used for fit is 400—750 nm. All the determination coefficients calculated for the exponential fits were always >0.9. All absorption subcomponent measurements are baseline corrected, assuming negligible absorption at 750 nm.

2.2. Models used in the study

2.2.1. Schofield's model
The optical signature inversion method (OSI) was developed Schofield et al., 2004) to invert the *in situ* absorption data collected using ac-9 to calculate weights of specific absorption coefficients for optical constituents present in the water column (Eq. (7)). Here the spectral absorption from ac-9 is the absorption after removal of absorption due to water, $a_{nw}(\lambda)$. Briefly, this model involves the calculation of weights (w_{1-5}) corresponding to three generalized phytoplankton absorption spectra $a_{ph\ 1-3}(\lambda)$ (Eq. 8), magnitudes and exponential slopes (S_d and S_g) of NAP matter and CDOM (Eq. (9) and (10)) using nonlinear constrained regression. The three $a_{ph\ 1-3}(\lambda)$ spectra correspond to generalized spectral absorption of chlorophyll *a—c*, phycobilin, and chlorophyll *a-b* containing phytoplankton, respectively, and were obtained from Johnsen et al. (1994). For both CDOM and NAP matter absorptions, a curve as a function of wave-

Table 1 Output variables from each absorption partitioning algorithm with reference. The parameters provided as model outputs are indicated by "X." The parameters not provided as output by a model are indicated by "-." For example, the SCM model provides $a_{ph}(\lambda)$ and $a_{dg}(\lambda)$ only as outputs and S_{dg} is calculated using $a_{dg}(\lambda)$.

Model	$a_{ph}(\lambda)$	$a_{dg}(\lambda)$	$a_d(\lambda)$	$a_g(\lambda)$	S_d	S_g	S_{dg}	Reference
GSCM	X	X	X	X	X	X	X	(Zheng et al., 2015)
Lin	X	X	X	X	X	X	X	(Lin et al., 2013)
Schofield	X	X	X	X	X	X	X	(Schofield et al., 2004)
SCM	X	X	-	-	-	-	X	(Zheng and Stramski, 2013a)
Zhang	X	X	-	-	-	-	X	(Zhang et al., 2015)

length and an exponential slope is used Eq. (9) and (10). The OSI method uses distinctive constraints on the weights of the phytoplankton, CDOM and NAP matter absorption coefficients. The constraints used on absorption coefficients are available from Schofield et al. (2004).

$$a_{nw}(\lambda) = a_{ph}(\lambda) + a_d(\lambda) + a_g(\lambda) \qquad (7)$$

$$a_{ph}(\lambda) = w_1 a_{ph1}(\lambda) + w_2 a_{ph2}(\lambda) + w_3 a_{ph3}(\lambda) \qquad (8)$$

$$a_g(\lambda) = w_4 \exp\left[-S_g(\lambda - \lambda_0)\right] \qquad (9)$$

$$a_d(\lambda) = w_5 \exp\left[-S_d(\lambda - \lambda_0)\right] \qquad (10)$$

The reference wavelength, λ_0 is set to 412 nm. The MATLAB inbuilt routine 'fmincon' function with a sequential quadratic programming method is used as the optimization procedure. The initial values for all weights are set to 0.001, and for S_g and S_d parameters, the values are set to 0.010 and 0.008 nm^{-1}, respectively. The output variables, along with a reference for each model, are presented in Table 1.

2.2.2. Lin's model

In a study by Lin et al. (2013), absorption subcomponents of water samples collected during eight cruises in the northern South China Sea and NASA bio-Optical Marine Algorithm Dataset (NOMAD) were used to model phytoplankton and particulate absorption coefficients ($a_p(\lambda)$, m^{-1}) as second-order quadratic empirical equations Eq. (11) and (12). The particulate absorption coefficient consists of absorption from both phytoplankton and NAP. The empirical equations exhibited good performance in representing empirical characteristics of phytoplankton and particulate coefficients (Lin et al., 2013).

$$a_{ph}(\lambda) = m_0(\lambda) a_{ph}(\lambda_0)^2 + m_1(\lambda) a_{ph}(\lambda_0) \qquad (11)$$

$$a_p(\lambda) = n_0(\lambda) a_p(\lambda_0)^2 + n_1(\lambda) a_p(\lambda_0) \qquad (12)$$

The reference wavelength (λ_0) used to reconstruct $a_{ph}(\lambda)$ and $a_p(\lambda)$ is set to 489 nm. The coefficients m_{0-1} and n_{0-1} are provided in Table 2 of Lin et al. (2013).

Based on these spectral Eq. (11) and (12) relationships, an APA was proposed to partition $a_{nw}(\lambda)$ into the absorption subcomponents in three steps. In the first step, $a_{nw}(\lambda)$ is partitioned into $a_{ph}(\lambda)$ and $a_{dg}(\lambda)$ with $a_{nw}(\lambda)$ expressed as Eq. (13).

$$
\begin{aligned}
a_{nw}(\lambda) &= m_0(\lambda) a_{ph}(\lambda_0)^2 + m_1(\lambda) a_{ph}(\lambda_0) \\
&\quad + a_{dg}(412) \exp\left[-S_{dg}(\lambda - 412)\right]
\end{aligned} \qquad (13)
$$

The optimal solution to Eq. (13) involves finding optimal values of $a_{ph}(\lambda_0)$, S_{dg} and $a_{dg}(412)$ while minimizing the error between modelled and measured $a_{nw}(\lambda)$. Initial estimates of the variables were set to 0.1 m^{-1}, 0.015 nm^{-1} and 0.2 m^{-1}, respectively. The values of $a_{ph}(\lambda_0)$ and $a_{dg}(412)$ are constrained to be greater than zero, and S_{dg} is constrained to vary between 0.008−0.03 nm^{-1}. The MATLAB inbuilt routine, Genetic Algorithms (GA) function is used as the optimization technique. The second step involves partitioning $a_{nw}(\lambda)$ into $a_p(\lambda)$ and $a_g(\lambda)$ with $a_{nw}(\lambda)$ expressed as Eq. (14).

$$
\begin{aligned}
a_{nw}(\lambda) &= n_0(\lambda) a_p(\lambda_0)^2 + n_1(\lambda) a_p(\lambda_0) \\
&\quad + a_g(412) \exp\left[-S_g(\lambda - 412)\right]
\end{aligned} \qquad (14)
$$

The optimal values of $a_g(412)$, $a_p(\lambda_0)$ and S_g are found by minimizing the same error function as in step-1. Initial estimates of $a_g(412)$, $a_p(\lambda_0)$ and S_g are set to 0.2 m^{-1}, 0.1 m^{-1} and 0.015 nm^{-1} respectively, and the same constraints in the first step are used here. In the final step, $a_p(\lambda)$ obtained in the second step is partitioned into $a_{ph}(\lambda)$ and $a_d(\lambda)$, with $a_p(\lambda)$ modelled as Eq. (15).

$$
\begin{aligned}
a_p(\lambda) &= m_0(\lambda) a_{ph}(\lambda_0)^2 + m_1 a_{ph}(\lambda_0) \\
&\quad + a_d(412) \exp\left[-S_d(\lambda - 412)\right]
\end{aligned} \qquad (15)
$$

The optimal values of $a_{ph}(\lambda_0)$, $a_d(412)$ and $S_d(412)$ are found by minimizing the error between modelled and $a_p(\lambda)$ from step-2. The initial estimates of $a_{ph}(\lambda_0)$, $a_d(412)$ and $S_d(412)$ are set to 0.1 m^{-1}, 0.2 m^{-1} and 0.010 nm^{-1}, respectively. As the accuracy of $a_{ph}(\lambda)$ from step-3 depends on the accuracy of $a_p(\lambda)$ derived in step-2, these values are discarded and only $a_{ph}(\lambda)$ from step-1 are provided as output.

2.2.3. Stacked Constraints Model (SCM)

The Stacked Constraints Model (SCM) was developed by Zheng and Stramski (2013a) to partition $a_{nw}(\lambda)$ into $a_{ph}(\lambda)$ and $a_{dg}(\lambda)$. The input for the model is a_{nw} at minimum six light wavelengths of 412, 443, 490, 510, 555 and 670 nm. This model was developed to address some of the existing limitations such as 1) requirement of additional ancillary inputs like Chlorophyll-*a* concentration or remote-sensing reflectance (Ciotti and Bricaud, 2006; Lee et al., 2002; Roesler et al., 1989); 2) applicability in particular coastal regions (Gallegos and Neale, 2002; Schofield et al., 2004); 3) assumption of a fixed S_{dg}; 4) use of a single fixed spectral shape or a linear combination of small number of predefined spectral shapes as in Schofield et al. (2004) and Ciotti and Bricaud (2006).

The SCM model is based on several inequality constraints determined from an extensive, quality-verified dataset covering a wide range of oceanic and coastal waters. This model is based on less restrictive assumptions about the spectral shape of $a_{ph}(\lambda)$ and S_{dg}. The less restrictive assumptions allow to adequately account for large variations in the spectral shape of $a_{ph}(\lambda)$ that can be possible due to phytoplankton community composition and acclimation to environmental conditions. The SCM model uses field-measured representative spectra shapes of $a_p(\lambda)$, $a_d(\lambda)$ and $a_g(\lambda)$ from various locations for the development of the model. The output from the model consists of a range of feasible solutions of $a_{ph}(\lambda)$ and $a_{dg}(\lambda)$ that satisfy the inequality constraints.

2.2.4. Generalized Stacked Constraints Model (GSCM)

GSCM (Zheng et al., 2015) is an extended approach to the SCM model and partitions $a_{nw}(\lambda)$ into $a_{ph}(\lambda)$, $a_d(\lambda)$ and $a_g(\lambda)$. The GSCM model is developed using the measured absorption subcomponents from the Chesapeake Bay, USA. In addition to the inequality constraints used in the SCM model, constraints pertaining to a_d spectra are applied in the GSCM model. Unlike Lin's and Schofield's models, GSCM uses representative spectral shapes for absorption subcomponents collected from the Chesapeake Bay. This model can be applied to other regions after performing modifications based on collected field data, especially to the library of representative shapes of absorption subcomponents. Performance evaluation of the GSCM model in optically complex coastal, estuarine and inland waters in other regions needs to be performed.

2.2.5. Zhang's model

A model developed by Zhang inverts $a_{nw}(\lambda)$ to infer phytoplankton size classes, chlorophyll concentration and CDM (Zhang et al., 2015). Three chlorophyll-specific absorption spectra $a_{pico}^*(\lambda)$, $a_{nano}^*(\lambda)$ and $a_{micro}^*(\lambda)$ corresponding to pico-, nano-, and micro- phytoplankton are used for modelling $a_{ph}(\lambda)$ (Uitz et al., 2008). The inversion involves two steps. In the first step, S_{dg} in Eq. (16) is fixed to an arbitrary value in the range [0.004, 0.02] nm^{-1} and a linear matrix inversion of the kernel comprising the three $a_{ph}^*(\lambda)$ and $a_{dg}^*(\lambda)$ (Eq. (18)) is performed. The weight m_1 corresponds to $a_{dg}(400)$ m^{-1} and the three weights m_{2-4} correspond to chlorophyll-*a* concentrations of pico-, nano- and micro-phytoplankton. In the second step, the optimal value of S_{dg} is found by minimizing the error between modelled a_{nw}^* and measured a_{nw}.

$$a_{dg}^*(\lambda) = \exp\left(-S_{dg}(\lambda - 500nm)\right) \tag{16}$$

$$a_{nw} = a_{nw}^* m \tag{17}$$

$$m = [m_1, m_2, m_3, m_4] \tag{18}$$

$$a_{nw}^* = \left[a_{dg}^*, a_{pico}^*, a_{nano}^*, a_{micro}^*\right] \tag{19}$$

To obtain the optimal value of S_{dg}, bounded global minimum search ('fminbnd' function of MATLAB) is used.

Lin's and Schofield's models provide S_d, S_g and S_{dg} as outputs. In the case of other models, slopes for absorption coefficients (a_d, a_g, a_{dg}) are obtained by fitting an exponential fit (Bricaud et al., 1981; Das et al., 2017; Twardowski et al., 2004) using a MATLAB code (Boss, 2014).

2.3. Statistical indicators

The statistical indicators used to assess the performance of five APA's are mean absolute percentage error (MAPE), mean absolute error (MAE), centered root mean squared errors (RMSD), standard deviation, correlation coefficient and percentage of valid retrievals (η).

$$MAPE = \left(\frac{100\%}{n}\right) \sum_{i=1}^{n} \left|(y_i - \widehat{y_i})/y_i\right|$$

$$MAE = \left(\frac{1}{n}\right) \sum_{i=1}^{n} \left|(y_i - \widehat{y_i})\right|$$

$$RMSD = \frac{1}{n} \sum_{i=1}^{n} \left[(y_i - y_{isd}) - (\widehat{y_i} - \widehat{y_{isd}})\right]^2$$

$$\eta = \frac{number\ of\ valid\ model - derived\ values}{number\ of\ valid\ observed\ values} X\ 100 \tag{20}$$

where y_i, $\widehat{y_i}$, y_{isd} and $\widehat{y_{isd}}$ represent the observed value, model-derived value, the standard deviation of observed values and standard deviation of model-derived values, respectively. The absorption subcomponents retrieved by various models are considered valid only when the values are greater than zero. The number of such valid data points are used for the calculation of η. Similarly, only positive values of measured absorption coefficients are considered valid (n).

Taylor diagrams (Joliff et al., 2009; Taylor, 2005, 2001) present a convenient way to compare various models in quantified terms of their correlation, standard deviations and RMSD's. The diagrams provide a view of the relative merit of one model over the other and hence are used to compare the performance of APAs for their retrieval capability of absorption subcomponents. In addition, a linear model is fit between model-derived and measured absorption subcomponents. A slope value close to one and a y-intercept value near zero indicates that model-derived values compare well with observed data.

3. Results

The input to five APA's is a_{nw} at seven wavelengths of 412, 443, 469, 490, 510, 555, and 670 nm and the absorption coefficients of subcomponents from the APA's are derived at these seven wavelengths only. Hereafter, the term "all wavelengths" implies these seven wavelengths.

3.1. Comparison of models in the retrieval of Phytoplankton absorption coefficient ($a_{ph}(\lambda)$)

The results of the comparison of five models in the retrieval of $a_{ph}(\lambda)$ is presented in Figure 3. For all models, MAPE values for retrieved a_{ph} at 443 and 670 nm are lower compared to the rest of the wavelengths. The highest MAPE values (Figure 3A) were observed at 555 nm compared to the rest of the wavelengths for all models. The average spectral MAPE (average of MAPE values across all wavelengths) for $a_{ph}(\lambda)$ retrieved by GSCM, SCM and Schofield models lie in the range of 26—29%. Lin and Zhang's models resulted in higher
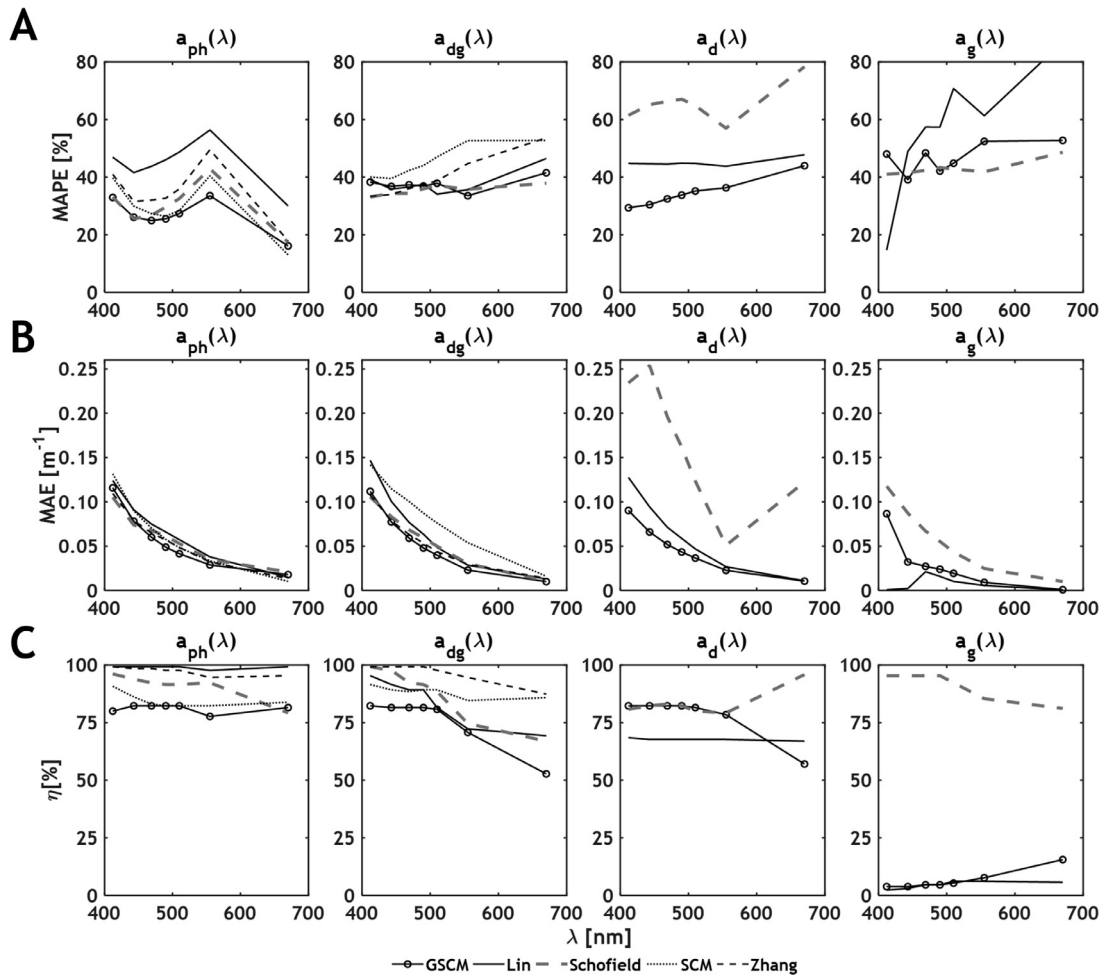
Figure 3 Comparison of (A) Spectral Mean Absolute Percentage Errors and (B) Percentage of valid retrievals η, for five models GSCM (Blackline with circular markers), Lin (black line), Schofield (grey thick dashed line), SCM (black dotted line) and Zhang (black dashed line) in the retrieval of spectral a_{ph}, a_{dg}, a_d and a_g. SCM and Zhang's models provide a_{ph} and a_{dg} spectra as outputs. Schofield, GSCM and Lin's models provide a_{ph}, a_{dg}, a_d and a_g spectra as outputs.

average spectral MAPE values of 44% and 34%, respectively, compared to the rest of the models. For the MAE statistic, all models exhibited a decreasing pattern with an increase in wavelength. The highest MAE values in the range 0.10—0.13 m^{-1} are observed at 412 nm and lowest values of the range 0.01—0.02 m^{-1} at 670 nm (Figure 3B). In the case of η (Figure 3C), a_{ph} retrieved by all models at all wavelengths are more than 75% valid. GSCM and SCM models derived $a_{ph}(\lambda)$ have slightly lower η as compared to Lin, Schofield and Zhang models. The comparison of models using the correlation coefficient, standard deviation and RMSD's is presented in Taylor diagrams (Figure 4). Average spectral RMSD for GSCM and SCM models are similar, i.e., 0.0645 m^{-1}.

Similarly, Zhang and Schofield's models obtained a similar average spectral RMSD of 0.0758 m^{-1}. Spectrally, all the models exhibited a decreasing trend with higher RMSD's in blue wavelengths (412 nm) to lower RMSD's in red wavelengths (670 nm) as observed in MAE. The average spectral correlation coefficients of GSCM (0.89), Lin (0.84), Schofield (0.84), SCM (0.89) and Zhang models (0.85) similar performance of all models. Based on all the statistics, GSCM, SCM and Schofield's models exhibited a better performance in the retrieval of $a_{ph}(\lambda)$ with lower errors but with a slightly

lower number of valid retrievals as compared to other models.

3.2. Comparison of models in the retrieval of the absorption coefficient of CDM ($a_{dg}(\lambda)$)

In retrieval $a_{dg}(\lambda)$ of , all models resulted in lower MAPE values in the blue-green wavelength region and increased towards the red wavelength region (Figure 3A). Higher MAPE values were observed at 670 nm as compared to the rest of the wavelengths. The average spectral MAPE for $a_{dg}(\lambda)$ retrieved by GSCM (37%), Schofield (35%), Lin (37%), Zhang (39%), and SCM (45%) models indicate better performance of Schofield, Lin and GSCM models. As observed in the case of $a_{ph}(\lambda)$, spectral MAE statistics for all models exhibit a decreasing pattern (Figure 3B). In the case of η (Figure 3C), SCM and Zhang models resulted in more than 85% valid retrievals at all wavelengths. The value of η for Lin, Schofield and GSCM models-derived a_{dg} is higher in blue-green wavelengths and decreased towards longer wavelengths, with the lowest η% observed at 670 nm. The comparison of models in retrieval of $a_{dg}(\lambda)$ using correlation coefficient, standard deviation and RMSD's is presented in Taylor diagrams
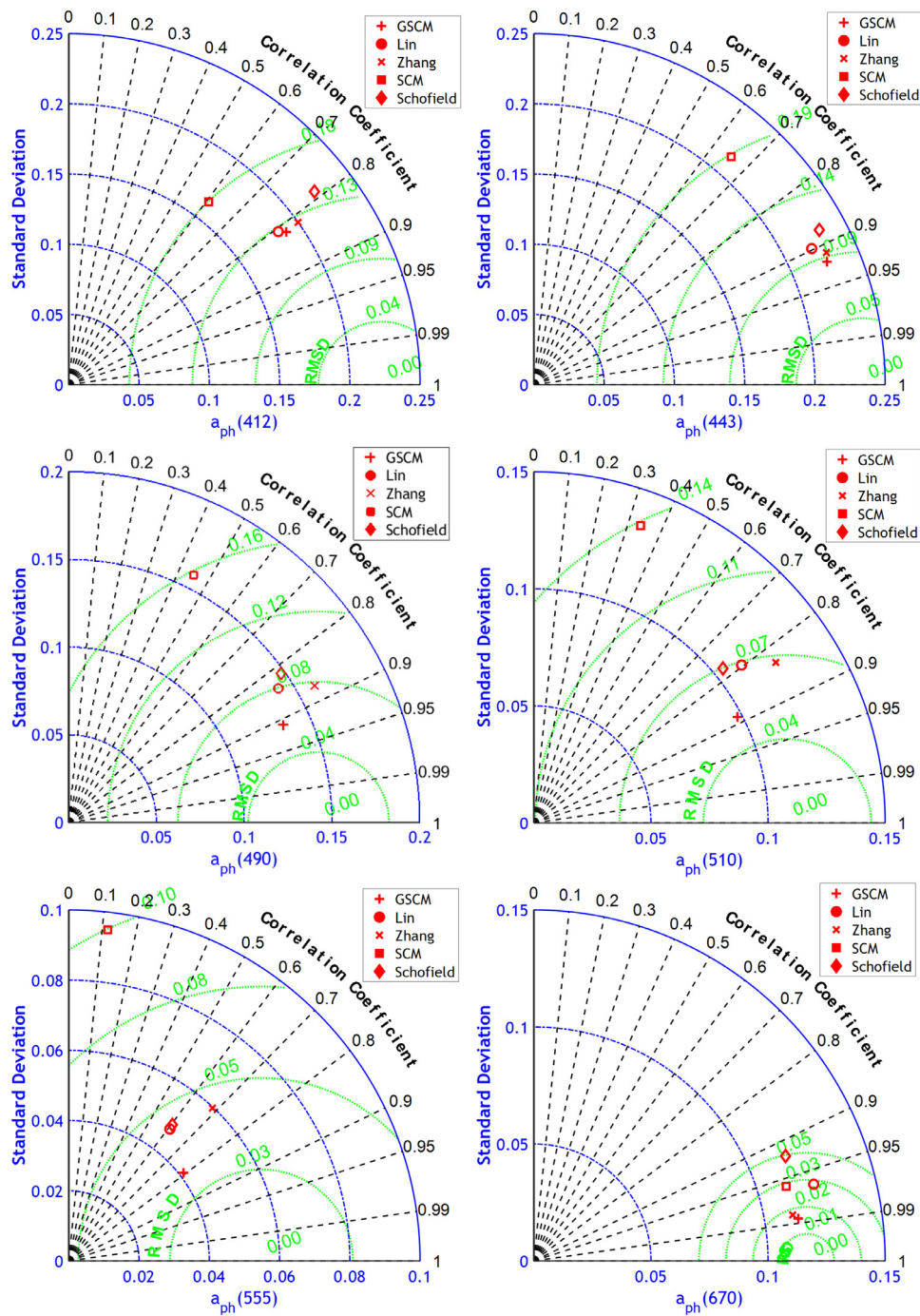
Figure 4   Taylor diagrams for a_{ph} at six light wavelengths (412, 443, 490, 510, 555, 670 nm) retrieved by GSCM, Lin, Zhang, SCM and Schofield models.

(Figure 5). The average spectral RMSD values of GSCM (0.064 m^{-1}), Zhang (0.073 m^{-1}) and Schofield (0.084 m^{-1}) models are lower as compared to Lin (0.126 m^{-1}) and SCM (0.146 m^{-1}) models. Similar to $a_{ph}(\lambda)$, all models exhibited a spectrally decreasing trend with an increase in wavelength. The average spectral correlation coefficients of GSCM (0.82), Lin (0.73), Schofield (0.88), SCM (0.42) and Zhang models (0.92) indicate better performance of GSCM, Schofield and Zhang models (Figure 5). Based on the error statistics, GSCM and Schofield's models exhibited similar overall performance.

3.3. Comparison of models in the retrieval of absorption coefficients of NAP ($a_d(\lambda)$) and CDOM ($a_g(\lambda)$)

GSCM, Lin's and Schofield's models provide a_d and a_g spectra as outputs along with a_{ph} and a_{dg} spectra. In the retrieval of $a_d(\lambda)$, among the three models, GSCM resulted in lower MAPE values with an average spectral MAPE of 34% compared to Lin (45%) and Schofield (65%) models (Figure 3A). Average spectral MAE for GSCM (0.057 m^{-1}) is also lower
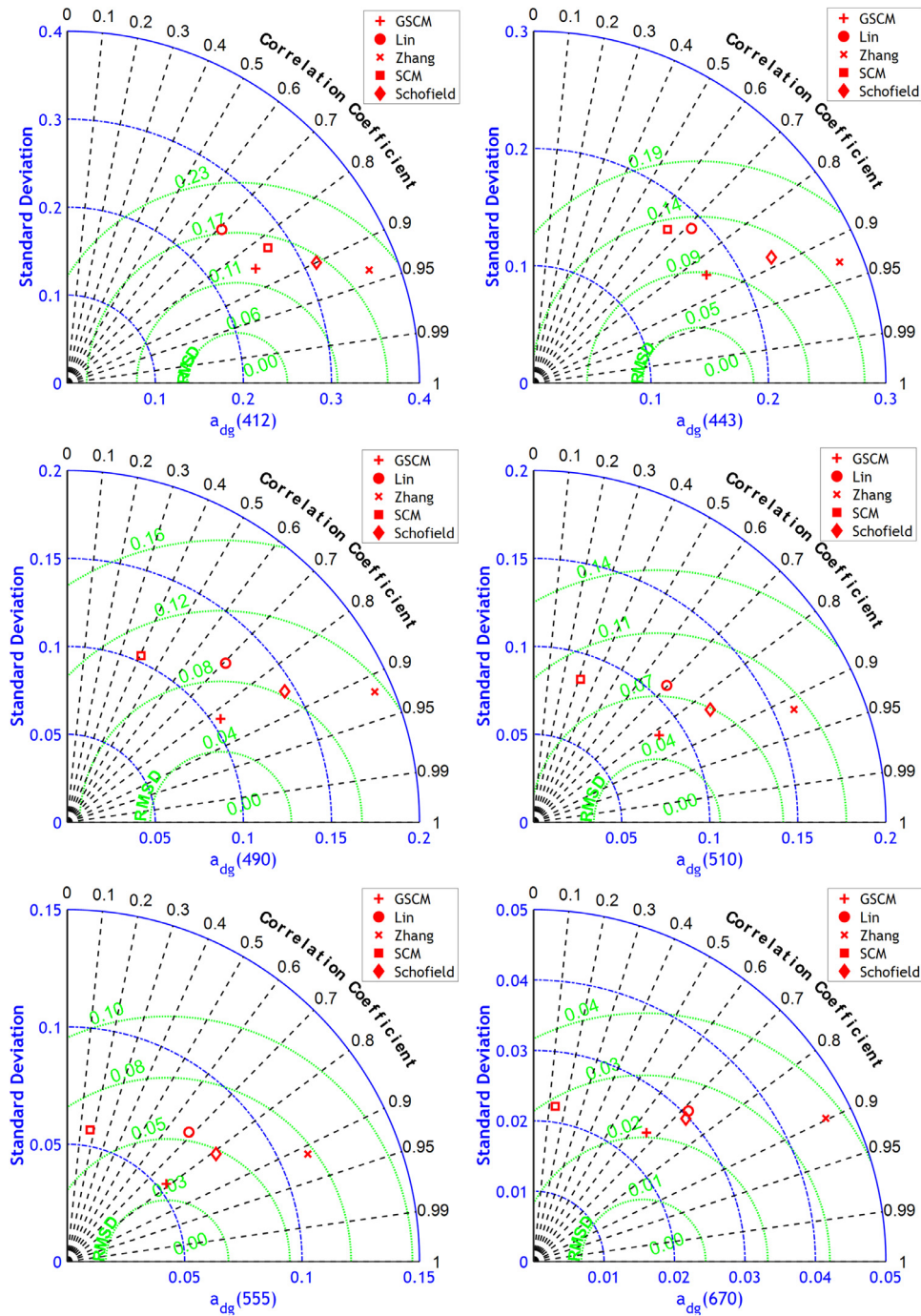
Figure 5 Taylor diagrams for a_{dg} at six light wavelengths (412, 443, 490, 510, 555, 670 nm) retrieved by GSCM, Lin, Zhang, SCM and Schofield models.

than Lin (0.066 m^{-1}) and Schofield (0.146 m^{-1}) models. Lin model-derived a_d have lower validity (67%) (Figure 3C), than Schofield's (82%) and GSCM (77%) model in 412—555 nm range. Table 2 presents the correlation coefficient, slope and y-intercept of linear model fit and RMSD's calculated for model-derived a_d and observed a_d values at seven wavelengths. GSCM model resulted in higher correlation coefficients (>0.75) at most of the wavelengths as compared to Lin and Schofield's models (Table 2).

The RMSD values for the GSCM model are lower compared to Lin's and Schofield's models at most of the wavelengths. Similarly, the linear fit slope for the GSCM model at various wavelengths ranges from 1.232 to 1.329 and closer to one. The slopes of linear fit for Lin's model (S ranges from 0.239 to 0.613) and Schofield's model (S ranges from 0.005 to 0.408) are far from one as compared to the GSCM model. Overall, GSCM model-derived a_d spectra obtained lower errors than Lin's and Schofield's models.

Table 2 Statistical indicators for a_d and a_g retrieved by GSCM, Lin and Schofield models at seven light wavelengths of 412, 443, 469, 490, 510, 555 and 670 nm. The values in italics in the case of r and RMSD statistics represent the best performing model with the highest r and lowest RMSD. A linear model is fit between model-derived and measured absorption subcomponents. A slope value close to one and a y-intercept value near zero indicates that the model-derived values compare well with observed data.

Model	Statistic	412	443	469	490	510	555	670
					a_d			
GSCM	*r*	*0.79*	*0.78*	*0.78*	*0.77*	*0.77*	*0.76*	*0.76*
Lin		0.41	0.40	0.38	0.37	0.37	0.37	0.40
Schofield		0.27	0.14	0.17	0.20	0.27	0.60	0.02
GSCM	**Slope**	*1.232*	*1.234*	*1.264*	*1.264*	*1.329*	*1.292*	*1.627*
Lin		0.613	0.554	0.495	0.442	0.424	0.406	0.239
Schofield		0.212	0.061	0.077	0.091	0.133	0.408	0.002
GSCM	**Y-**	-0.0976	-0.0609	-0.0439	-0.0329	-0.0278	-0.0110	-0.0111
Lin	**intercept**	*-0.0151*	*-0.0011*	*0.0076*	*0.0108*	*0.0105*	*0.0089*	*0.0046*
Schofield		0.0638	0.0838	0.0603	0.0470	0.0328	0.0001	0.0167
GSCM	**RMSD**	*0.115*	*0.086*	*0.068*	*0.057*	*0.048*	*0.030*	0.015
Lin	**[m^{-1}]**	0.135	0.099	0.077	0.063	0.051	0.032	*0.012*
Schofield		0.219	0.234	0.174	0.139	0.103	0.042	0.114
					a_g			
		412	443	469	490	510	555	670
GSCM	*r*	0.91	0.89	0.90	0.89	0.88	0.87	0.85
Lin		*0.99*	*0.97*	*0.98*	*0.98*	*0.98*	*0.98*	*1.00*
Schofield		0.75	0.71	0.69	0.67	0.66	0.65	0.61
GSCM	**Slope**	0.711	0.587	0.528	0.481	0.452	0.445	0.594
Lin		1.606	1.633	1.557	1.507	1.487	1.429	1.697
Schofield		*1.266*	*1.311*	*1.321*	*1.290*	*1.340*	*1.101*	*0.853*
GSCM	**Y-**	*-0.0148*	-0.0094	-0.0131	-0.0103	-0.0059	*-0.0037*	-0.0017
Lin	**intercept**	-0.0254	*-0.0080*	*-0.0015*	*0.0006*	*0.0048*	0.0038	*-0.0006*
Schofield		-0.1182	-0.0941	-0.0718	-0.0566	-0.0497	-0.0150	-0.0020
GSCM	**RMSD**	0.174	0.150	0.122	0.104	0.088	0.054	*0.011*
Lin	**[m^{-1}]**	*0.113*	*0.093*	*0.069*	*0.054*	*0.044*	*0.027*	0.014
Schofield		0.144	0.111	0.088	0.073	0.060	0.033	0.012

In retrieval of $a_g(\lambda)$, Schofield's model resulted in lower MAPE values with an average spectral MAPE of 42% compared to Lin (56%) and GSCM (46%) models (Figure 3A). The η values (Figure 3C) from Lin (4%), GSCM (6%), and Schofield (90%) indicate that most of Lin and GSCM model-derived $a_g(\lambda)$ are invalid.

Lin's model-derived a_g exhibited the lowest RMSD at most of the wavelengths, possibly owing to least η. In the case of slopes of the linear fit, Schofield's model obtained S values closer to one than Lin and GSCM models. Similar to lower RMSD values, higher correlation coefficients obtained for GSCM and Lin's models-derived $a_g(\lambda)$ can be a result of the lowest η. Overall, Schofield's model-derived $a_g(\lambda)$ has lower errors and the highest η% as compared to Lin and GSCM models (Table 2).

The ratio of model-derived IOPs to observed IOPs of a_{ph}, a_{dg}, a_d and a_g at seven light wavelengths of 412, 443, 469, 490, 510, 555 and 670 nm are presented in Figure 6. If the model-derived IOPs are closer to observed IOPs, the ratios will be closer to one, leading to a median

value closer to one. Therefore, a model that exhibits a median of ratios closer to one indicates better performance than models with a median of ratios far from one. In the case of $a_{ph}(\lambda)$ (model-derived/observed) ratio (Figure 6A), the deviation of median values (from one) of all models increased in 443—555 nm range. A similar pattern is observed in the spectral MAPE values of $a_{ph}(\lambda)$ (Figure 3A) with higher MAPE values at 555 nm among all wavelengths.

Similar to the spectral MAE trend observed for $a_{dg}(\lambda)$ (Figure 3), the deviation in the median values of a_{dg} (model-derived/observed) ratio increased with an increase in wavelength with higher deviations observed at 670 nm. This trend implies that the model-derived a_{dg} are closer to observed a_{dg} at 412 and 443 nm and the deviation from observed a_{dg} increased with increase in wavelength. In the case of $a_d(\lambda)$ (model-derived/observed) ratios, the median values of the GSCM model, are closer to one, indicating better performance than Lin and Schofield's models. These results agree with lower error statistics observed for GSCM
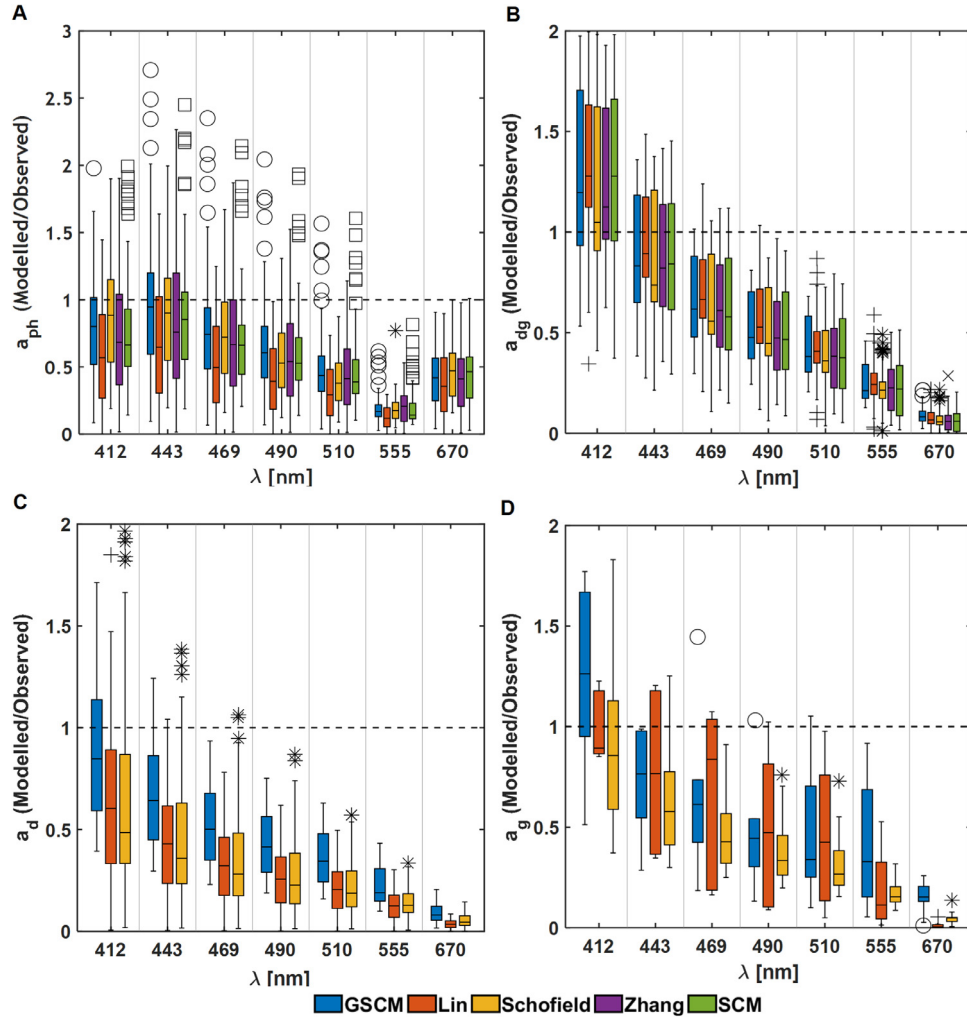
Figure 6 Box and whiskers plots of the ratio of model-derived IOPs to observed IOPs, (A) $a_{ph}(\lambda)$, (B) $a_{dg}(\lambda)$, (C) $a_d(\lambda)$, and (D) $a_g(\lambda)$ at seven light wavelengths of 412, 443, 469, 490, 510, 555 and 670 nm. A grey dashed line is used to indicate a ratio value of one. SCM and Zhang's models provide a_{ph} and a_{dg} spectra as outputs. Schofield, GSCM and Lin's models provide a_{ph}, a_{dg}, a_d and a_g spectra as outputs. The centre of each box indicates the median of the values, the top and bottom are the 25th and 75th percentage of samples, length of the box indicates the interquartile range. The outliers in model outputs are indicated by a circle, plus, square, cross and asterisk above and below the whiskers.

model-derived $a_d(\lambda)$. For the ratio of model-derived and observed $a_g(\lambda)$ values (Figure 6D), median values from Lin's and Schofield's models are closer to one as compared to GSCM.

3.4. Comparison of models in the retrieval of slopes of absorption subcomponents, CDOM (S_g), NAP (S_d) and CDM (S_{dg})

GSCM model-derived S_{dg} obtained the least MAPE of ˜8% compared to the rest of the models (Figure 7). Zhang's model-derived S_{dg} has a higher validity of 99% but with a higher MAPE of 23%. All the models can derive S_{dg} with η more than 80%. Except for Zhang's model, the slopes of the linear fits from other models are far from one. A possible reason for for this deviation could be resulting from the limited range of variation observed in S_dg values. All model-derived S_{dg} have lower correlation coefficients.

The model-derived S_d vs. observed S_d for GSCM, Lin and Schofield's models are presented in Figure 8A. MAPE values for Lin and Schofield's models in the retrieval of S_d coefficients are 7% and 19% as compared to 22% obtained for the GSCM model. Schofield's model resulted in the highest 93.8% valid S_d retrievals as compared to Lin's (69.2%) and GSCM (86.9%). The slope and y-intercept of the linear fit between model-derived and observed S_d values of GSCM model are closer to one and zero as compared to the Lin and Schofield models. The lowest MAPE obtained by Lin's model could result from the least $\eta\%$ values among the three models. Overall, GSCM model-derived S_d obtained the highest r, S value closer to one and >85% valid η. All the models exhibited poor performance in retrieval of S_g parameter, i.e., lower r and η (Figure 8B) were obtained as compared to the statistics obtained in the retrieval of S_d and S_{dg} coefficients.

Overall, GSCM model-derived a_{ph}, a_{dg}, a_d and S_d have lower errors than the rest of the models. Schofield's model also exhibited good performance with a higher number of
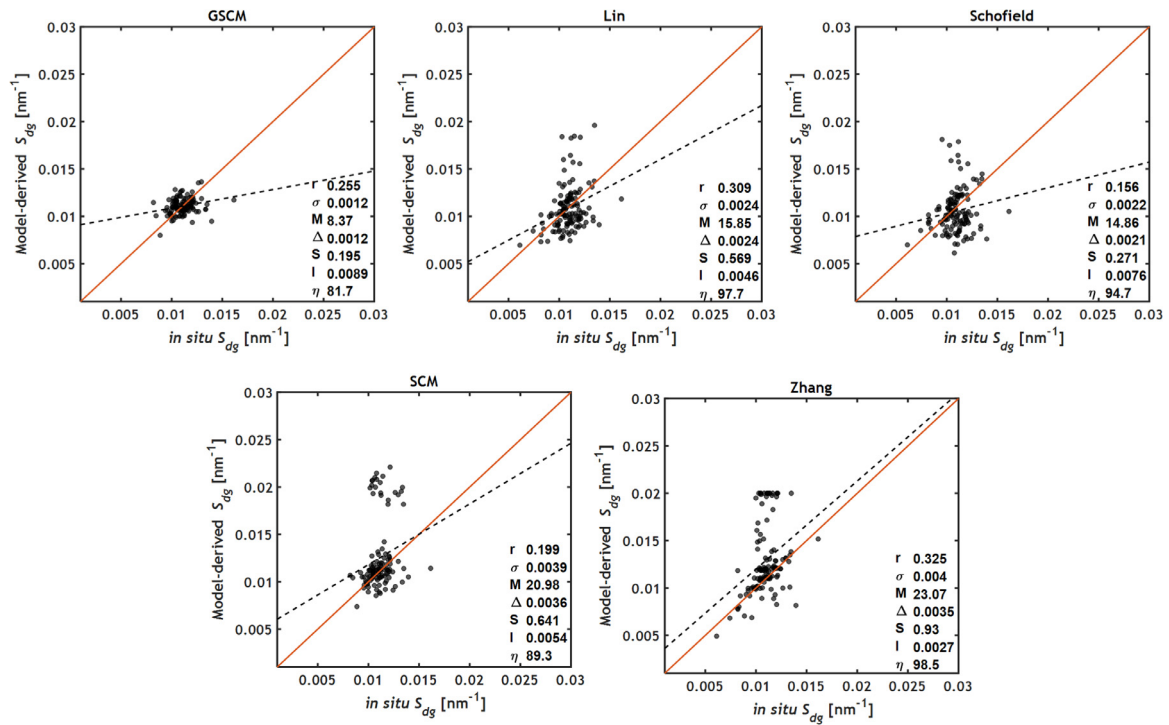
Figure 7 Model-derived vs. *in situ* S_{dg} retrieved by five models — GSCM, Lin, Schofield, SCM and Zhang. The statistics r — Correlation coefficient, σ — Standard deviation, M — Mean Absolute Percentage Error in %, Δ — Centred root-mean-square difference, S and I — Slope and Intercept of the linear fit and η is in %, calculated as (number of valid retrievals/number of valid observed values) × 100. The solid red line indicates a 1:1 line, and the black dotted line represents the linear fit between model-derived and *in situ* measured slope.
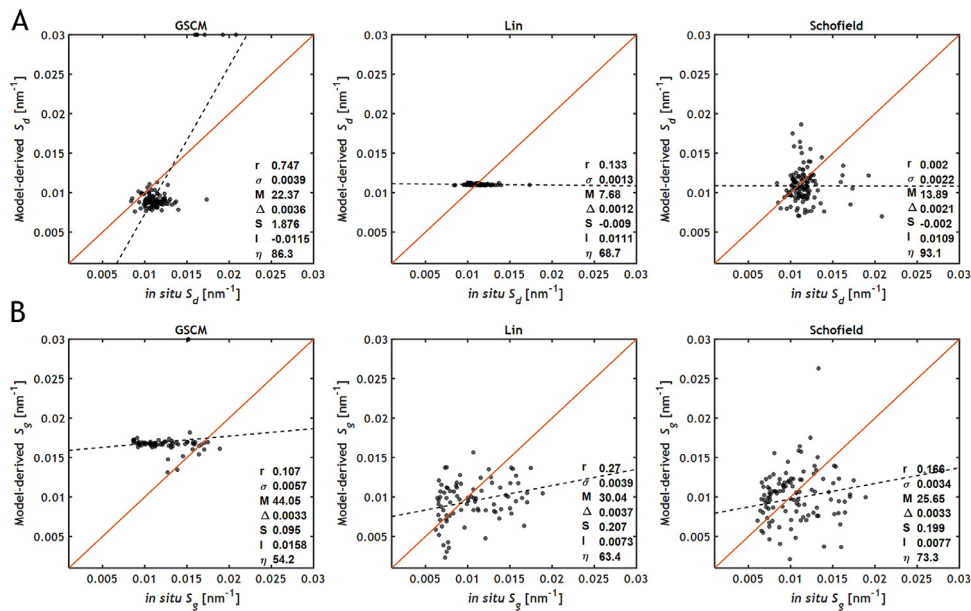
Figure 8 Model-derived vs. *in situ* (A) S_d and (B) S_g retrieved by GSCM, Lin and Schofield models. The statistics r — Correlation coefficient, σ — Standard deviation, M — Mean Absolute Percentage Error in %, Δ — Centred root-mean-square difference, S and I — Slope and Intercept of the linear fit and η is in %, calculated as (number of valid retrievals/number of valid observed values) × 100. The solid red line indicates a 1:1 line, and the black dotted line represents the linear fit between model-derived and *in situ* measured slope.

Table 3 Statistical indicators for S_g, S_d and S_{dg} derived from GSCM, Lin and Schofield's models. Each of the five models is compared for their slope parameters retrieval performance with the application of 1). Baseline correction (BLC) to $a_{ph}(\lambda)$ and $a_g(\lambda)$ only and 2). BLC to $a_{ph}(\lambda)$, $a_d(\lambda)$ and $a_g(\lambda)$. Values of statistical indicators in italics indicate the better performing model.

Model	Statistic Slope coefficient	BLC for $a_{ph}(\lambda)$, $a_d(\lambda)$ and $a_g(\lambda)$			BLC only for $a_{ph}(\lambda)$ and $a_g(\lambda)$		
		S_{dg}	S_d	S_g	S_{dg}	S_d	S_g
GSCM	MAPE [%]	*8.37*	*22.37*	*44.05*	37.71	23.00	44.48
	MAE [m^{-1}]	*0.0009*	0.0028	0.0048	0.0023	*0.0019*	*0.0047*
	r	0.26	0.75	0.11	*0.74*	*0.82*	0.05
	Slope	0.195	1.876	0.095	*0.738*	*1.817*	0.224
	Y-intercept	0.0089	-0.0115	0.0158	*0.0039*	*-0.0053*	0.0138
	RMSD	*0.0012*	0.0036	*0.0033*	0.0014	*0.0032*	0.0036
	$\eta\%$	*82.3*	*86.9*	54.6	73.3	82.4	55.7
Lin	MAPE [%]	*15.85*	*7.68*	*30.04*	23.46	45.99	47.15
	MAE [m^{-1}]	0.0018	*0.0009*	*0.0031*	*0.0014*	0.0032	0.0052
	r	0.31	0.13	0.27	*0.76*	-0.43	0.14
	Slope	0.569	-0.009	0.207	1.100	-0.018	0.352
	Y-intercept	0.0046	0.0111	0.0073	0.0002	0.0112	0.0020
	RMSD	0.0024	*0.0012*	*0.0037*	*0.0016*	0.0021	0.0042
	$\eta\%$	*98.5*	*69.2*	*63.8*	76.3	48.9	62.6
Schofield	MAPE [%]	*14.86*	*13.89*	25.65	22.29	22.90	*23.76*
	MAE [m^{-1}]	0.0017	*0.0017*	0.0028	*0.0015*	0.0018	*0.0023*
	r	0.16	0.002	0.17	*0.67*	*0.71*	0.38
	Slope	0.271	-0.002	0.199	*1.014*	*0.709*	1.509
	Y-intercept	0.0076	0.0109	0.0077	0.0004	0.0030	-0.0051
	RMSD	0.0021	*0.0021*	0.0033	*0.0017*	0.0022	*0.0028*
	$\eta\%$	*95.4*	*93.8*	*73.8*	63.4	76.3	49.6
SCM	MAPE [%]	*20.98*	-	-	46.44	-	-
	MAE [m^{-1}]	*0.0025*	-	-	0.0031	-	-
	r	0.2	-	-	0.67	-	-
	Slope	0.641	-	-	1.461	-	-
	Y-intercept	0.0054	-	-	-0.0005	-	-
	RMSD	0.0036	-	-	*0.0021*	-	-
	$\eta\%$	*90*	-	-	52.3	-	-
Zhang	MAPE [%]	23.07	-	-	29.50	-	-
	MAE [m^{-1}]	0.0024	-	-	*0.0019*	-	-
	r	0.33	-	-	0.73	-	-
	Slope	0.93	-	-	0.571	-	-
	Y-intercept	0.0027	-	-	0.0049	-	-
	RMSD	0.0036	-	-	0.0015	-	-
	$\eta\%$	*99.2*	-	-	40.0	-	-

valid retrievals and errors for the derived absorption subcomponents a_{ph}, a_{dg} and a_d comparable with GSCM. None of the models exhibited good performance in deriving S_g parameter.

3.5. Effect of baseline correction of a_d spectra on model performance

All the absorption subcomponent data were baseline corrected before used as input to performance evaluation of models. Baseline correction (BLC) significantly affects the performance of models in deriving absorption subcomponents. In the case of a robust signal in NIR, the application of baseline correction may reduce the magnitude of absorption

at all wavelengths. Hence, to understand the effect of baseline correction of a_d, the entire analysis is repeated without correcting a_d (Figures 9 and 10, Table 3).

Baseline correction of a_d affects each model's absorption subcomponent retrieval performance differently, owing to distinctive methodologies (Figure 9).

Without BLC correction for $a_d(\lambda)$, GSCM, SCM and Zhang's models exhibited a balanced change, i.e., average spectral MAPE for the retrieved $a_{ph}(\lambda)$ increased combined with a decrease in average spectral MAPE for the retrieved $a_{dg}(\lambda)$. Lin and Schofield's model-derived $a_{dg}(\lambda)$ obtained $\sim$10% lower average spectral MAPE without BLC correction for $a_d(\lambda)$ compared to data with BLC corrected $a_d(\lambda)$. If $a_d(\lambda)$ is not BLC corrected, $\eta\%$ for the derived $a_{ph}(\lambda)$ decreased combined with an increased η for derived
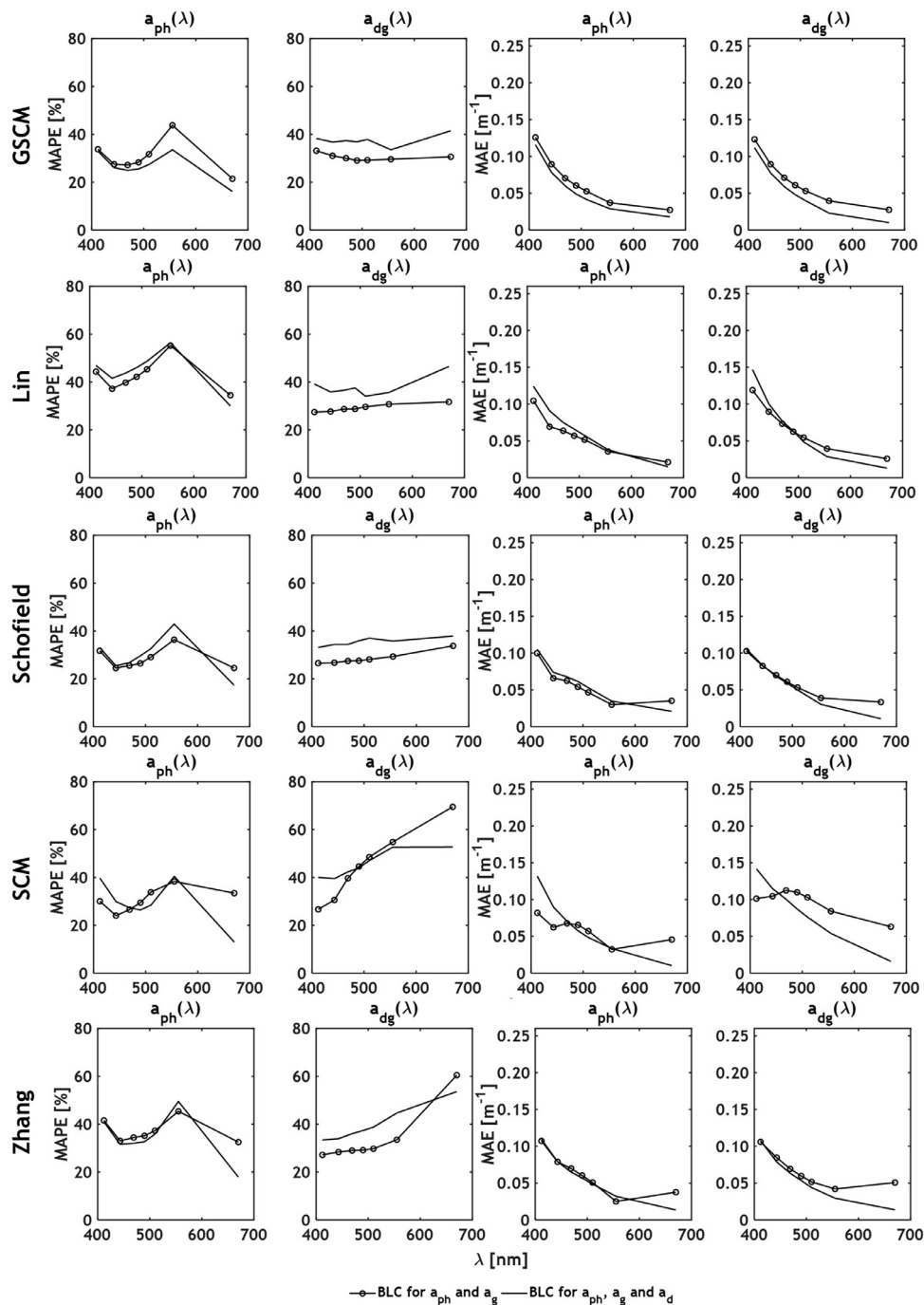
Figure 9 MAPE and MAE statistics for $a_{ph}(\lambda)$ and $a_{dg}(\lambda)$ derived from GSCM, Lin, Schofield, SCM and Zhang models. The five models are compared for their absorption subcomponent retrieval performance with the application of 1) baseline correction (BLC) to $a_{ph}(\lambda)$ and $a_g(\lambda)$ only and 2) BLC to $a_{ph}(\lambda)$, $a_d(\lambda)$ and $a_g(\lambda)$.

$a_{dg}(\lambda)$, thereby indicating a balancing pattern as observed in MAPE.

The average spectral MAPE for GSCM model-derived $a_d(\lambda)$ decreased while using uncorrected $a_d(\lambda)$ (Figure 10). In the case of Lin's model, the average spectral MAPE value for the derived $a_d(\lambda)$ increased by ~8% while using uncorrected $a_d(\lambda)$. BLC of $a_d(\lambda)$ didn't have a significant effect on the GSCM and Schofield model-derived $a_g(\lambda)$. For Lin's model, average spectral MAPE for the derived $a_g(\lambda)$ decreased by

~8% when uncorrected $a_d(\lambda)$ is used, thereby balancing the increase in average spectral MAPE observed in $a_d(\lambda)$. The $\eta\%$ for $a_d(\lambda)$ and $a_g(\lambda)$ retrievals changed by less than 2%.

MAPE values for S_{dg} derived from all models using uncorrected $a_d(\lambda)$ are 8—30% higher than using baseline-corrected $a_d(\lambda)$ data (Table 3). Similarly, $\eta\%$ for the derived S_{dg} decreased by 8—50% when uncorrected $a_d(\lambda)$ data is used by all models. Lin and Schofield's model-
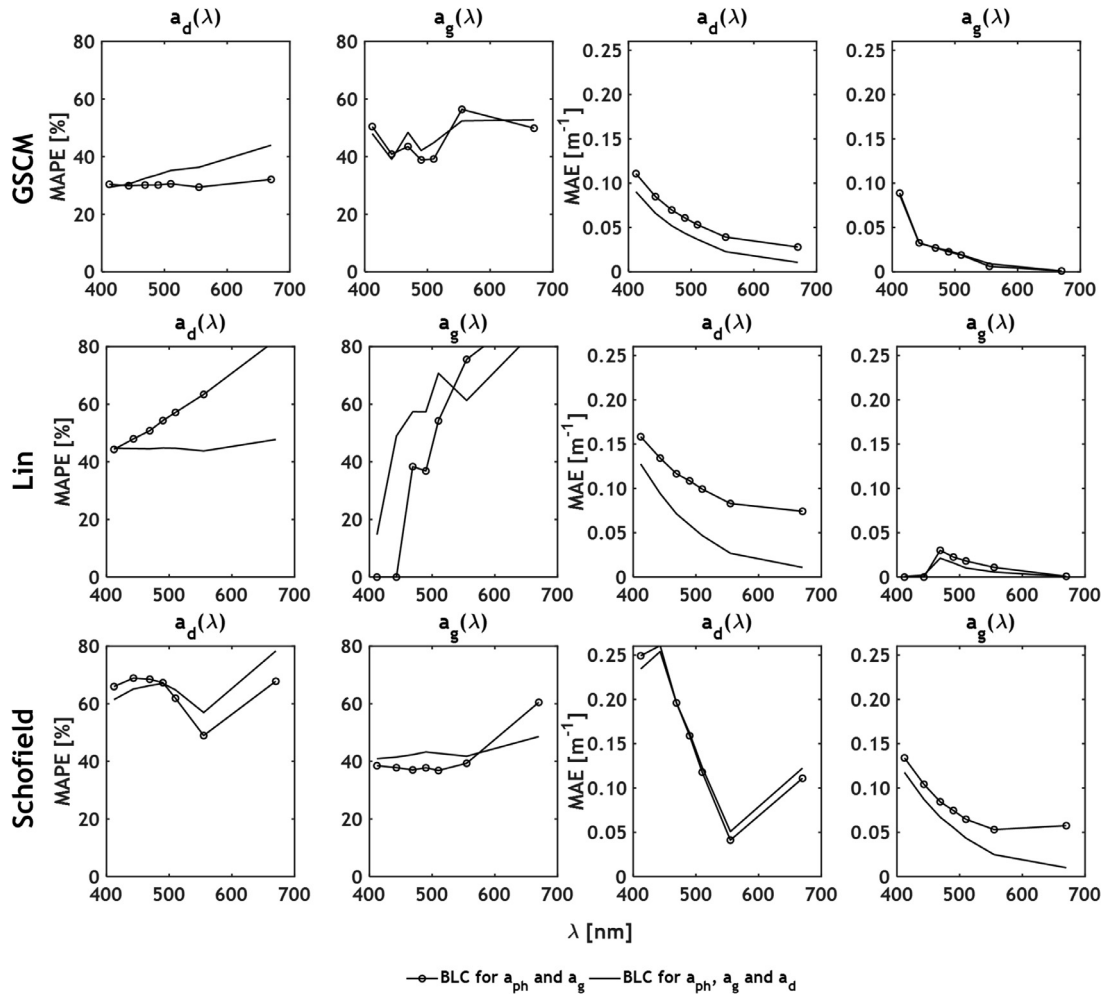
Figure 10 MAPE and MAE statistics for $a_d(\lambda)$ and $a_g(\lambda)$ derived from GSCM, Lin and Schofield models. The three models are compared for their absorption subcomponent retrieval performance with the application of 1) Baseline correction (BLC) to $a_{ph}(\lambda)$ and $a_g(\lambda)$ only and 2) BLC to $a_{ph}(\lambda)$, $a_d(\lambda)$ and $a_g(\lambda)$.

derived $S_d(\lambda)$ have 9% and 38% lower MAPE values when BLC $a_d(\lambda)$ is used. Similar to S_{dg}, higher $\eta\%$ are obtained when $a_d(\lambda)$ data is baseline corrected. Lin's model-derived S_g obtained 17% lower MAPE in using baseline-corrected $a_d(\lambda)$. Based on the observed errors and percentage of valid retrievals for the derived absorption subcomponents and slope coefficients, using baseline-corrected data is suggested.

4. Discussion

This paper focuses on evaluating the performance of a variety of absorption partitioning algorithms. The models were evaluated using a dataset covering sites Kochi and Goa coastal waters of India. The higher concentrations of CDOM and NAP material resulting from terrestrial runoff and coastal sediment re-suspension increase optical complexity of both sites. An increase in optical complexity increases the difficulty in partitioning $a_{nw}(\lambda)$ into absorption subcomponents, especially in deriving a_d and a_g components with greater accuracy. One of the critical points in comparing the

models using this dataset is that none of the models were parameterized based on Kochi and Goa coastal waters data, thus providing an independent evaluation. As the present study focuses on the applicability of APAs in coastal waters, their performance comparison in the open ocean is out of scope and can be pursued in further studies. The absorption measurements of phytoplankton and NAP material were made implementing the QFT, wherein the first step is the measurement of $a_p(\lambda)$ and the second step involves subjecting the sample filter to depigmentation treatment. The coefficient $a_{ph}(\lambda)$ is then calculated as the difference between $a_p(\lambda)$ and $a_d(\lambda)$. Although QFT provides reasonable estimates of $a_{ph}(\lambda)$, some uncertainties that can induce an error in absorption measurements are incomplete removal of phytoplankton pigments or removing pigments that do not belong to phytoplankton. This incomplete or excess removal can contribute to the mismatch between desired and measured absorption coefficients of $a_p(\lambda)$ and $a_{ph}(\lambda)$ (Zheng and Stramski, 2013a,b). Apart from the QFT method, the absorption measurements can be obtained from absorption measuring devices like ac-9. However, these measurements can be affected by several factors like temperature, salinity and

scattering. Even with the best available methods for correcting the errors and biases due to the factors mentioned above, the residual error can be 20% or more. Further, the absorption estimates can be less accurate and may contain higher errors in red and NIR wavelengths owing to a greater contribution of water absorption (Stockley et al., 2017).

In addition to the APAs evaluated in the present study, other APAs that require ancillary inputs like chlorophyll-*a* concentration or remote sensing reflectance also exist (Ciotti and Bricaud, 2006; Lee et al., 2002; Roesler et al., 1989). The use of additional inputs apart from $a_{nw}(\lambda)$ can induce some additional errors and uncertainties, thereby increasing the complexity in the evaluation of APAs. The five models evaluated for their IOP retrieval capabilities are not devoid of limitations. In the case of Lin's model, $a_{ph}(\lambda)$ is parameterized as a quadratic function developed based on a large set of *in situ* data, however, this parameterization limits the variation in its spectral shape. Another limitation of the model is the generation of two sets of $a_{ph}(\lambda)$ and $a_d(\lambda)$ that are not identical, thereby resulting in an incomplete closure. In all the three models, the absorption subcomponents of $a_d(\lambda)$, $a_g(\lambda)$ and $a_{dg}(\lambda)$ were modelled using a single spectral exponential shape. Such parameterization could fail to represent potential variations in the slope as a function of wavelength in a given spectrum, especially for S_g (Loiselle et al., 2009; Zheng and Stramski, 2013a). To overcome these existing limitations, the SCM model was proposed that allows for flexibility in the spectral shapes of both $a_{ph}(\lambda)$ and $a_{dg}(\lambda)$, and with less restrictive assumptions about the slopes of $a_{dg}(\lambda)$. Although this model was developed using a large *in situ* dataset covering a wide range of optical properties, its performance in extreme cases is limited. The coastal waters of Goa represents such an extreme case wherein NAP and CDOM absorption dominates phytoplankton absorption and hence, the performance of SCM model is limited (Figure 3). The GSCM model was proposed to cover the coastal and estuarine waters (sediment and CDOM rich) and also relaxes the assumption of exponential function for $a_{dg}(\lambda)$ in SCM model. Unlike SCM model, GSCM uses a library of spectral shapes to describe the shape of $a_{dg}(\lambda)$. Although GSCM model resulted in a lower number of valid retrievals, the IOPs retrieved resulted in lower errors as observed in Figure 3 and Figure 7. The Zhang's model was developed with emphasis on retrieval of the phytoplankton size classes. The datasets used to evaluate Zhang's model cover both oceanic and coastal regimes, however, the $a_{ph}(443)$ in these datasets is higher compared to the $a_{dg}(443)$ range. For example, the range of $a_{dg}(400)$ observed in the NOMAD dataset used to evaluate Zhang's model is low with a range of 0.01—0.6 m^{-1} as compared to the dataset used in the present study with a range of 0.08—2.99 m^{-1}. Although Zhang's model resulted in a higher number of valid retrievals of $a_{ph}(\lambda)$ and $a_{dg}(\lambda)$ among all other models, it also resulted in higher MAPE values (Figure 3). Both SCM and GSCM models provide the flexibility for tuning with *in situ* data with respect to inequality constraints, library shapes and boundaries for better retrieval of IOPs. In the case of Schofield's, Lin's and Zhang's models, the variations in the spectral shapes of $a_{ph}^*(\lambda)$ are fixed along with assumption of exponential shape for $a_{dg}(\lambda)$.

5. Conclusions

In this study, we evaluated the applicability of five absorption partitioning algorithms in partitioning $a_{nw}(\lambda)$ into separate component absorption coefficients of $a_{ph}(\lambda)$, $a_d(\lambda)$ and $a_g(\lambda)$ or into $a_{ph}(\lambda)$ and $a_{dg}(\lambda)$. The five APAs (Schofield's, Lin's, SCM, GSCM and Zhang's models) were evaluated on a dataset comprising optically complex waters collected from two sites, Kochi and Goa coastal waters of India. The evaluation of APAs in CDOM and NAP-rich waters (as in this study) is necessary to check their capability in retrieving the absorption subcomponents and slope parameters. The input to the models is a_{nw} measured at seven light wavelengths of 412, 443, 469, 490, 510, 555 and 670 nm present in most remote-sensing and *in situ* platforms. The SCM and Zhang's models provide $a_{ph}(\lambda)$ and $a_{dg}(\lambda)$, whereas the remaining models, i.e., GSCM, Lin's and Schofield's models, provide $a_{ph}(\lambda)$, $a_d(\lambda)$ and $a_g(\lambda)$ coefficients.

In the retrieval of $a_{ph}(\lambda)$, the average spectral MAPE values of all the models lie in the range of 26—44%. Among the five models, GSCM, SCM and Schofield's models exhibited better performance than the rest with lower average spectral MAPE and higher correlation coefficient values. In the case of $a_{dg}(\lambda)$ retrievals, average spectral MAPE values of the GSCM (37%), Lin (37%), Schofield's (35%) models were lower than the rest of the models that resulted in average spectral MAPE values in the range of 39—45%. In the case of $a_d(\lambda)$ retrievals, the GSCM model exhibited a lower average spectral MAPE of 34% as compared to Lin's (45%) and Schofield's (65%) models. The average spectral MAPE values in the retrieval of $a_g(\lambda)$ for Lin's (56%), Schofield's (42%) and GSCM (46%) indicate better performance of Schofield's model compared to Lin's and GSCM models. All models exhibited good performance in the retrieval of S_{dg} MAPE values in the range of 8—23%. However, the correlation coefficients obtained for the linear fit between modelled and measured S_{dg} from all the models (except Zhang) is less than 0.65. GSCM model-derived S_d coefficients are >85% valid, with the highest *r* of 0.75. None of the models demonstrated good performance in deriving S_g. Overall, the GSCM model resulted in a good performance in the retrieval of the absorption subcomponents, $a_{ph}(\lambda)$, $a_{dg}(\lambda)$, $a_d(\lambda)$ and the S_d in coastal waters of Kochi and Goa. Next, Schofield's model exhibited good performance in retrieval of $a_{ph}(\lambda)$, $a_{dg}(\lambda)$ and $a_g(\lambda)$. Baseline correction of NAP absorption data profoundly impacts the errors and number of valid retrievals of the derived absorption subcomponents and slope coefficients. Results indicate that performing BLC on NAP absorption data varied the performance of each model differently. Based on the results, use of uncorrected NAP data reduced the number of valid slope coefficient retrievals. The performance of the remaining models may further be improved by tuning the models with *in situ* data. Further improvements are necessary to achieve reasonable accuracy in the retrieval of $a_g(\lambda)$ and S_g. As the present study deals with Kochi and Goa sites only, these models need to be tested in other sites to check the ability of the models in the retrieval of absorption coefficients of subcomponents.

Declaration of competing interests

There are no potential competing interests.

Acknowledgments

References

ac Meter Protocol Document, 2011. Rev. Q, Wet Labs.

Boss, E., 2014. Software to compute the spectral slope of dissolved absorption (exponential fit). MISC Lab, Univ. Maine.

Brewin, R.J.W., Sathyendranath, S., Müller, D., Brockmann, C., Deschamps, P.Y., Devred, E., Doerffer, R., Fomferra, N., Franz, B., Grant, M., Groom, S., Horseman, A., Hu, C., Krasemann, H., Lee, Z.P., Maritorena, S., Mélin, F., Peters, M., Platt, T., Regner, P., Smyth, T., Steinmetz, F., Swinton, J., Werdell, J., White, G.N., 2015. The Ocean Colour Climate Change Initiative: III. A round-robin comparison on in-water bio-optical algorithms. Remote Sens. Environ. 162, 271–294. https://doi.org/10.1016/j.rse.2013.09.016

Bricaud, A., Ciotti, A.M., Gentili, B., 2012. Spatial-temporal variations in phytoplankton size and colored detrital matter absorption at global and regional scales, as derived from twelve years of SeaWiFS data (1998-2009). Global Biogeochem. Cy. 26, 1–17. https://doi.org/10.1029/2010GB003952

Bricaud, A., Morel, A., Babin, M., Allali, K., Claustre, H., 1998. Variations of light absorption by suspended particles with chlorophyll a concentration in oceanic (case 1) waters : Analysis and implications for bio-optical models. J. Geophys. Res. 103, 31033–31044.

Bricaud, A., Morel, A., Prieur, L., 1981. Absorption by dissolved organic matter of the sea (yellow substance) in the UV and visible domains. Limnol. Oceanogr. 26, 43–53. https://doi.org/10.4319/lo.1981.26.1.0043

Ciotti, A.M., Bricaud, A., 2006. Retrievals of a size parameter for phytoplankton and spectral light absorption by colored detrital matter from water-leaving radiances at SeaWiFS channels in a continental shelf region off Brazil. Limnol. Oceanogr. Methods 4, 237–253. https://doi.org/10.4319/lom.2006.4.237

Ciotti, M., Lewis, M.R., Cullen, J.J., 2002. Assessment of the relationships between dominant cell size in natural phytoplankton communities and the spectral shape of the absorption coefficient. Limnol. Oceanogr. 47, 404–417.

Cleveland, J.S., Weidemann, A.D., 1993. Quantifying absorption by aquatic particles: A multiple scattering correction for glass-fiber filters. Limnol. Oceanogr. 38, 1321–1327. https://doi.org/10.4319/lo.1993.38.6.1321

Dana, D.R., Maffione, R.A., 2006. A New Hyperspectral Spherical—Cavity Absorption Meter. In: AGU Ocean Sciences Meeting, Honolulu, Hawaii, 1–13.

Das, S., Das, I., Giri, S., Chanda, A., Maity, S., Lotliker, A.A., Kumar, T.S., Akhand, A., Hazra, S., 2017. Chromophoric dissolved organic matter (CDOM) variability over the continental shelf of the northern Bay of Bengal. Oceanologia 59 (3), 271–282. https://doi.org/10.1016/j.oceano.2017.03.002

Freeman, S., 2012. Calibration and data processing of acs device.

Gallegos, C.L., Neale, P.J., 2002. Partitioning spectral absorption in case 2 waters: discrimination of dissolved and particulate components. Appl. Opt. 41, 4220–4233. https://doi.org/10.1364/ao.41.004220

Green, S.A., Blough, N.V., 1994. Optical absorption and fluorescence properties of chromophoric dissolved organic matter in natural waters. Limnol. Oceanogr. 39, 1903–1916. https://doi.org/10.4319/lo.1994.39.8.1903

Grunert, B.K., Mouw, C.B., Ciochetto, A.B., 2018. Characterizing CDOM Spectral Variability Across Diverse Regions and Spectral Ranges. Global Biogeochem. Cy. 32, 57–77. https://doi.org/10.1002/2017GB005756

Johnsen, G., Samset, O., Granskog, L., Sakshaug, E., 1994. In vivo absorption characteristics in 10 classes of bloom-forming phytoplankton — Taxonomic characteristics and responses to photoadaptation by means of discriminant and HPLC analysis. Mar. Ecol. Prog. Ser. 105, 149–158. https://doi.org/10.3354/meps105149

Joliff, J.K., Kindle, J.C., Shulman, I.G., Penta, B., Friedrichs, M.A.M., Helber, R., Arnone, R.A., 2009. Summary diagrams for coupled hydrodynamic-ecosystem model skill assessment. J. Marine Syst. 76, 64–82.

Kishino, M., Takahashi, M., Okami, N., Ichimura, S., 1985. Estimation of the spectral absorption coefficients of phytoplankton in the sea. Bull. Mar. Sci. 37, 634–642.

Kowalczuk, P., Kaczmarek, S., 1996. Analysis of temporal and spatial variability of yellow substance absorption in the southern baltic. Oceanologia 38 (1), 1–32.

Kyewalyanga, M.N., Platt, T., Sathyendranath, S., 1998. Seasonal variations in physiological parameters of phytoplankton across the North Atlantic. J. Plankt. 20, 17–42.

Lee, Z., Carder, K.L., Arnone, R.A., 2002. Deriving inherent optical properties from water color: a multiband quasi-analytical algorithm for optically deep waters. Appl. Opt. 41, 5755–5772. https://doi.org/10.1364/AO.41.005755

Lin, J., Cao, W., Wang, G., Hu, S., 2013. Approach for determining the contributions of phytoplankton, colored organic material, and nonalgal particles to the total spectral absorption in marine waters. Appl. Opt. 52, 4249–4257. https://doi.org/10.1364/AO.52.004249

Loiselle, S.A., Bracchini, L., Dattilo, A.M., Ricci, M., Tognazzi, A., Cózar, A., Rossi, C., 2009. Optical characterization of chromophoric dissolved organic matter using wavelength distribution of absorption spectral slopes. Limnol. Oceanogr. 54, 590–597. https://doi.org/10.4319/lo.2009.54.2.0590

Lotliker, A.A., Baliarsingh, S.K., Kumar, T.S., 2016. Satellite Coastal and Oceanographic Research Inter-comparison Exercise (SICOME).

Mason, J.D., Cone, M.T., Fry, E.S., 2016. Ultraviolet (250–550 nm) absorption spectrum of pure water. Appl. Opt. 55, 7163. https://doi.org/10.1364/ao.55.007163

Menon, H.B., Adhikari, A., 2018. Remote Sensing of Chlorophyll-A in Case II Waters: A Novel Approach With Improved Accuracy Over Widely Implemented Turbid Water Indices. J. Geophys. Res. Ocean. 123, 8138–8158. https://doi.org/10.1029/2018JC014052

Menon, H.B., Lotliker, A., Nayak, S.R., 2005. Pre-monsoon bio-optical properties in estuarine, coastal and Lakshadweep waters. Estuar. Coast. Shelf Sci. 63, 211–223. https://doi.org/10.1016/j.ecss.2004.11.015

Menon, H.B., Sangekar, N.P., Lotliker, A.A., Vethamony, P., 2011. Dynamics of chromophoric dissolved organic matter in Mandovi and Zuari estuaries - A study through *in situ* and satellite data. ISPRS J. Photogramm. Remote Sens. 66, 545–552. https://doi.org/10.1016/j.isprsjprs.2011.02.011

Minu, P., Lotliker, A.A., Shaju, S.S., Ashraf, P.M., Kumar, T.S., Meenakumari, B., 2016. Performance of operational satellite bio-optical algorithms in different water types in the southeast-

ern Arabian Sea. Oceanologia 58 (4), 317—326. https://doi.org/10.1016/j.oceano.2016.05.005

Minu, P., Lotliker, A.A., Shaju, S.S., SanthoshKumar, B., Ashraf, P.M., Meenakumari, B., 2014. Effect of optically active substances and atmospheric correction schemes on remote-sensing reflectance at a coastal site off Kochi. Int. J. Remote Sens. 35, 5434—5447. https://doi.org/10.1080/01431161.2014.926420

Minu, P., Shaju, S.S., Souda, V.P., Usha, B., Ashraf, P.M., Meenakumari, B., 2015. Hyperspectral Variability of Phytoplankton Blooms in Coastal Waters off Kochi, South-eastern Arabian Sea. Fish. Tech. 52, 218—222.

Mitchell, B.G., 1990. Algorithms for determining the absorption coefficient for aquatic particulates using the quantitative filter technique. Ocean Opt. X 1302, 137. https://doi.org/10.1117/12.21440

Mobley, C.D., 2010. Light and Radiometry. Ocean Opt. Web B. 1—9.

Nimit, K., Lotlikar, A., Srinivasa Kumar, T., 2016. Validation of MERIS sensor's CoastColour algorithm for waters off the west coast of India. Int. J. Remote Sens. 37, 2066—2076. https://doi.org/10.1080/01431161.2015.1129564

Oubelkheir, K., Claustre, H., Bricaud, A., Babin, M., 2007. Partitioning total spectral absorption in phytoplankton and colored detrital material contributions. Limnol. Oceanogr. Methods 5, 384—395. https://doi.org/10.4319/lom.2007.5.384

Pope, R.M., Fry, E.S., 1997. Absorption spectrum (380—700nm) of pure water. II. Integrating cavity measurements. Appl. Opt. 36, 8710—8723.

Roesler, C.S., Perry, M.J., Carder, K.L., 1989. Modeling *in situ* phytoplankton absorption from total absorption spectra in productive inland marine waters. Limnol. Oceanogr. 34, 1510—1523.

Röttgers, R., Häse, C., Doerffer, R., 2007. Determination of the particulate absorption of microalgae using a point-source integrating-cavity absorption meter: Verification with a photometric technique, improvements for pigment bleaching, and correction for chlorophyll fluorescence. Limnol. Oceanogr. Methods 5, 1—12. https://doi.org/10.4319/lom.2007.5.1

Schofield, O., Bergmann, T., Oliver, M.J., Irwin, A., Kirkpatrick, G., Bissett, W.P., Moline, M.A., Orrico, C., 2004. Inversion of spectral absorption in the optically complex coastal waters of the Mid-Atlantic Bight. J. Geophys. Res. C Ocean. 109, 1—12. https://doi.org/10.1029/2003JC002071

Souda, V.P., Minu, P., Lotliker, A.A., Shaju, S.S., Ashraf, P.M., 2020. Inter-annual variability in the inherent optical properties along the southeastern Arabian Sea from 2009 to 2015. Arab. J. Geosci. 13. https://doi.org/10.1007/s12517-020-5063-z

Stockley, N.D., Röttgers, R., McKee, D., Lefering, I., Sullivan, J.M., Twardowski, M.S., 2017. Assessing uncertainties in scattering correction algorithms for reflective tube absorption measure-ments made with a WET Labs ac-9. Opt. Express 25, A1139—A1153. https://doi.org/10.1364/oe.25.0a1139

Taylor, K.E., 2005. Taylor Diagram Primer. Work. Pap.

Taylor, K.E., 2001. Summarizing multiple aspects of model performance in a single diagram. J. Geophys. Res. 106, 7183—7192. https://doi.org/10.1029/2000JD900719

Twardowski, M.S., Boss, E., Sullivan, J.M., Donaghay, P.L., 2004. Modeling the spectral shape of absorption by chromophoric dissolved organic matter. Mar. Chem. 89, 69—88. https://doi.org/10.1016/j.marchem.2004.02.008

Twardowski, M.S., Rottgers, R., Stramski, D., 2018. Chapter 1: The Absorption Coefficient, An Overview. In: Ocean Optics & Biogeochemistry Protocols for Satellite Ocean Colour Sensor Validation, 1—15.

Uitz, J., Huot, Y., Bruyant, F., Babin, M., Claustre, H., 2008. Relating phytoplankton photophysiological properties to community structure on large scales. Limnol. Oceanogr. 53, 614—630.

Wollschläger, J., Grunwald, M., Röttgers, R., Petersen, W., 2013. Flow-through PSICAM: A new approach for determining water constituents absorption continuously. Ocean Dyn. 63, 761—775. https://doi.org/10.1007/s10236-013-0629-x

Zaneveld, J.R.V., 2013. Fifty years of inherent optical properties. Methods Oceanogr. 7, 3—20. https://doi.org/10.1016/j.mio.2014.03.002

Zhang, X., Huot, Y., Bricaud, A., Sosik, H.M., 2015. Inversion of spectral absorption coefficients to infer phytoplankton size classes, chlorophyll concentration, and detrital matter. Appl. Opt. 54, 5805—5816. https://doi.org/10.1364/AO.54.005805

Zheng, G., Digiacomo, P.M., 2017. Remote sensing of chlorophyll-a in coastal waters based on the light absorption coefficient of phytoplankton. Remote Sens. Environ. 201, 331—341. https://doi.org/10.1016/j.rse.2017.09.008

Zheng, G., Stramski, D., 2013a. A model based on stacked-constraints approach for partitioning the light absorption coefficient of seawater into phytoplankton and non-phytoplankton components. J. Geophys. Res. Ocean. 118, 2155—2174. https://doi.org/10.1002/jgrc.20115

Zheng, G., Stramski, D., 2013b. A model for partitioning the light absorption coefficient of suspended marine particles into phytoplankton and nonalgal components. J. Geophys. Res. Ocean. 118, 2977—2991. https://doi.org/10.1002/jgrc.20206

Zheng, G., Stramski, D., Digiacomo, P.M., 2015. A model for partitioning the light absorption coefficient of natural waters into phytoplankton, nonalgal particulate, and colored dissolved organic components: A case study for the Chesapeake Bay. J. Geophys. Res. Ocean. 120, 2601—2621. https://doi.org/10.1002/2014JC010604